AIMS Materials Science, 4(1): 158-171.
DOI: 10.3934/matersci.2017.1.158
Received: 08 September 2016
Accepted: 10 January 2017
Published: 18 January 2017

http://www.aimspress.com/journal/Materials

Research article

Novel $ZnWO_4$/RGO nanocomposite as high performance photocatalyst

Mohamed Jaffer Sadiq Mohamed and Denthaje Krishna Bhat *

Department of Chemistry, National Institute of Technology Karnataka, Surathkal, Mangalore-575025, Karnataka, India

*** Correspondence:** Email: denthajekb@gmail.com; Tel: 0824-2473202.

Abstract: In this study, we report the synthesis of nanocomposite material composed of zinc tungstate ($ZnWO_4$) and reduced graphene oxide (RGO) as photocatalyst by a simple microwave irradiation technique. The prepared nanocomposites have been characterized by X-ray diffraction (XRD), transmission electron microscopy (TEM), energy dispersive X-ray (EDX) analysis, X-ray photoelectron spectroscopy (XPS), Fourier transform infrared spectrometer (FTIR), photoluminescence spectroscopy (PL) and UV-Visible spectroscopy. The photocatalytic activities of the prepared nanocomposites are evaluated in terms of the efficiencies of photodegradation of methylene blue (MB) dye in aqueous solution under visible light irradiation. The prepared nanocomposites showed excellent photodegradation efficiency compared to the commercial TiO_2 under visible light irradiation. The activity of the catalyst towards methyl orange (MO) and rhodamine B (RB) was also good. Further, in view of the low cost, simple preparation method and high catalytic activity of the material, it is expected that the prepared nanocomposite can serve as an environment friendly photocatalyst for treating the large scale industrial waste waters.

Keywords: photocatalyst; $ZnWO_4$/RGO; photocatalysis; microwave irradiation; methylene blue

1. Introduction

Many dyes that are being widely used in various industries such as paper, leather and textiles have become major source of environment pollution. The discharged industrial wastewaters containing dyes are source of serious threat to environment and health due to their toxicity, biodegradation and chemical stability [1]. Various technologies are developed for the removal of dye effluents from wastewater including membrane filtration, chemical oxidation, coagulation, adsorption and extraction [2]. Unfortunately, most of the present strategies developed for treatment

of industrial wastewater still have problems like low stability, high cost, poor efficiency [3]. Recent studies are devoted to the major use of photocatalysis for the treatment of dyes from wastewaters because of the advantage of this method over others.

Metal tungstates are one of the most used materials for photocatalysis. Among metal tungstates, owing to its stability, reactivity and molecular versatility, $ZnWO_4$ has been used widely in various fields such as gas sensor, X-ray, solid-state laser, g-scintillator, photocatalyst [4]. The photocatalytic performance of the semiconductor materials can be improved by compositing them with carbon materials [5]. Graphene, CNT and activated carbon are the carbonaceous material which have been widely used in various applications like electronics, optics, catalysts and biomaterials field [6]. Among them graphene has attracted more attention in developing materials for photocatalysis because of their excellent mechanical, thermal strength, highly ordered structure and high specific surface area [7]. For example, Wang et al. have reported the synthesis of RGO-$ZnWO_4$ nanocomposite for photocatalysis [8] and a recently reported synthesis of RGO-$ZnWO_4$-Fe_3O_4 nanocomposite for visible light photocatalysis from our group [9,10,11]. Inspired by these publications and as a part of our ongoing research work on tungstate based photocatalysts, we report herein investigation on the photocatalytic activity of the $ZnWO_4$/RGO nanocomposite photocatalyst with varied amount of RGO for the photodegradation of organic dyes MB, MO and RB in a suspension system. The synthesis method used here is more simple and the observed results are also two times better than the reported one [8].

2. Materials and Method

2.1. Materials

All the chemicals were purchased from Sigma Aldrich and were of analytical grade. These materials were used as received without any further purification. All the reactions were carried out using deionized water.

2.2. Synthesis of $ZnWO_4$/RGO Nanocomposites

One step microwave irradiation method was used to synthesize the $ZnWO_4$/RGO-x (x = 1, 2, 3 and 4 wt% GO) nanocomposite. Typically, the nomenclature $ZnWO_4$/RGO-3% refers to 100 g of $ZnWO_4$ and 3 g of GO respectively in the composite. GO was synthesized by modified Hummers method [12]. To prepare $ZnWO_4$/RGO nanocomposites, a given quantity of GO was dispersed in ethylene glycol solution using sonication for 30 minutes and 0.05 M of zinc acetate solution (50 mL) was slowly added to the dispersed GO solution. Later 0.05 M sodium tungstate solution (50 mL) was added to the above mixture under constant stirring for about 2 hours and maintained at pH = 9 using ammonia. Subsequently, the mixture was irradiated with microwave at 350 W for 10 minutes and the reaction mixture was cool down to room temperature naturally. The blackish precipitate collected was washed with 10% ethanol and dried in vacuum oven at 80 °C for 12 hours. The prepared samples were denoted as ZWRG-1%, ZWRG-2%, ZWRG-3% and ZWRG-4%, respectively, with the number referring to the weight ratios of added GO. Similar approach was carried out to synthesize pure $ZnWO_4$ (denoted as ZW) without adding GO solution and reduced graphene oxide (denoted as RGO) without adding $ZnWO_4$. Among the samples, ZWRG-3% showed the best results

for photodegradation of dyes. Hence this sample was adjudged as optimized sample and subjected for further characterizations.

2.3. Characterization

The purity and phase structure was determined by XRD (Rigaku, Japan) using Cu K_α (λ = 0.154 nm) radiation with a nickel filter over a 2θ range of 5–60° with a scan rate of 1°·min^{-1}. The morphology and elemental compositions of the prepared catalyst were examined by TEM (JEOL, USA), EDX analysis (SEM equipped with EDX, JEOL, USA) operated at 20 kV and X-ray photoelectron spectroscopy (XPS, Multilab 2000, UK). FT-IR spectra were recorded using a Fourier transform infrared spectrometer (Bruker). Room temperature photoluminescence spectrum was measured with 380 nm excitation wavelength source (LS-55, Perkin Elmer Instruments). Absorbance spectrum of the catalyst was obtained by using UV-Visible spectrophotometer (Analytik Jena).

2.4. Determination of Photocatalytic Activity

The photocatalytic activities of ZWRG nanocomposites were investigated using an aqueous solution of MB. The catalytic reactions were carried out using 500 mL Pyrex glass beaker with 100 mL of aqueous solution of 10 mg/L of MB in a photoreactor equipped with a 250 W Hg lamp (cut off filter 400 nm) as a source of visible light irradiation. To avoid heating of solutions during experiments, water was circulated around the photoreactor. 10 mg of the photocatalyst was added to the dye solution and stirred for about 30 minutes to reach the adsorption-desorption equilibrium. For photocatalytic studies, at specified time intervals, 4 mL of the reacted MB solution was withdrawn, centrifuged and UV-Visible spectrum was recorded at a wavelength of 664 nm. Further, to investigate the practical applications of the obtained samples on different organic pollutants such as MO and RB dyes, photocatalytic degradation studies were carried out with these dyes and the prepared nanocomposite employing same experimental procedure at wavelengths 554 nm and 464 nm, respectively. The percentage of degradation of dye was calculated from the following equation.

$$\text{Percentage of degradation of dye} = (C_0 - C)/C \times 100$$

where, C_0 is the initial absorbance of the dye solution and C is the absorbance at interval time "t".

3. Results and Discussion

3.1. Characterization of Nanocomposites

The XRD patterns of RGO, ZW and ZWRG-3% nanocomposites are shown in Figure 1. The diffraction peaks at 22.6° and 42.6° could be ascribed to reflections from (002) and (100) planes of RGO sheets conforming to JCPDS No. 01-0646. In the case of $ZnWO_4$, the diffraction peaks can be indexed to the monoclinic sanmartinite phase (JCPDS card no. 15-0774) of $ZnWO_4$, with space group P2/c (no. 13) with lattice parameter a = 4.691 Å, b = 5.720 Å, c = 4.925 Å and β = 90.64°. However, the ZWRG-3% nanocomposite did not show any diffraction peak corresponding to RGO. This may be due to the small percentage (3%) of RGO present in the sample. Further, no other

impurity peaks were observed in the XRD pattern. The existence of RGO in the composites could be confirmed by FTIR, TEM and XPS results shown later.

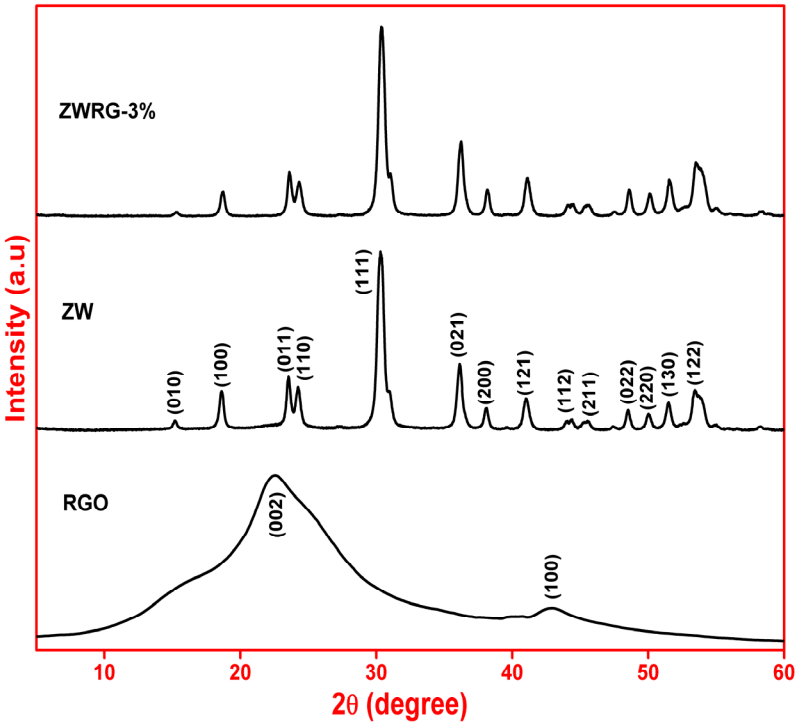

Figure 1. XRD patterns of RGO, ZW and ZWRG-3% nanocomposites.

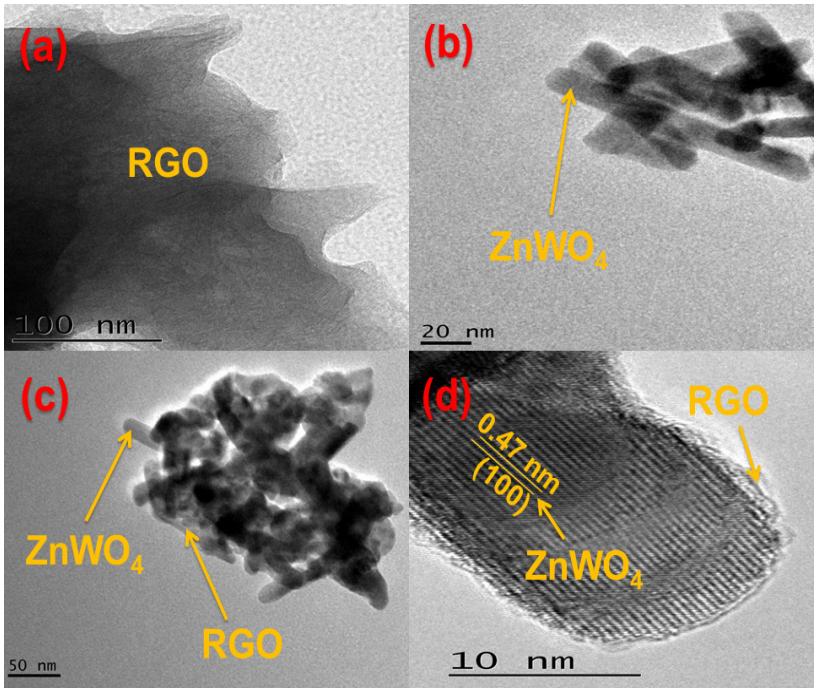

Figure 2. TEM images of (a) RGO, (b) ZW, (c) ZWRG-3% and (d) HRTEM image of ZWRG-3% nanocomposite.

Figure 2 reveals the morphological features of the as-prepared nanocomposites. Layered feature of RGO sheets can be seen in Figure 2a. TEM image in Figure 2b shows rod like ZW particles and in Figure 2c the ZW particles being anchored on the surface of the RGO sheets can be observed. The particles had their length in the range of 40 to 120 nm and width in the range of 10 to 20 nm with an average aspect ratio of 4. Figure 2d shows the HRTEM image of ZWRO-3% wherein, the incorporated ZW on the surface of the RGO nanosheets can be seen. The lattice fringes of 0.47 nm correspond to the (100) plane of $ZnWO_4$. Thus, it is evident that the interface is formed by the $ZnWO_4$ (100) plane on the surface of the RGO sheets. Further, the elemental analysis of the nanocomposites carried out by EDX analysis is shown in Figure S1. In the EDX spectra only C, O, Zn and W elements are found indicating that no impurities are present in the prepared nanocomposites.

FTIR spectra of the as-prepared RGO, ZW and ZWRG-3% nanocomposites are shown in Figure 3. The absorption band at 588 cm^{-1} corresponds to symmetric deformations of W–O in WO_6 octahedron structure [13]. The band at 722 cm^{-1} can be indexed to symmetrical vibration of bridged O atoms of the Zn–O–W [14]. The absorption bands at 823, 891 and 997 cm^{-1} are due to the vibration of the WO_2 units in the W_2O_8 group [14]. Further, absorption bands at 1367 and 1720 cm^{-1} can be attributed to bending vibrations of O–H corresponds to surface adsorbed water molecules on $ZnWO_4$, respectively [15,16]. In the spectra of RGO, the broad bands centred at 1225 cm^{-1} can be attributed to the C–O stretching vibration of the epoxy groups from the reduced GO sheets [17]. Moreover, the broad band at 1563 cm^{-1} corresponding to C=C skeletal vibration of RGO sheets can be a support for reduction of GO to RGO sheets [18]. The absorption frequencies observed in neat ZW slightly decreased in the composite due to physical adsorption interactions with the RGO. Similarly, the frequencies of neat RGO get slightly increased in the composite due to same reason. Thus, the FTIR spectral studies establish the interactions occurring in the composite formed.

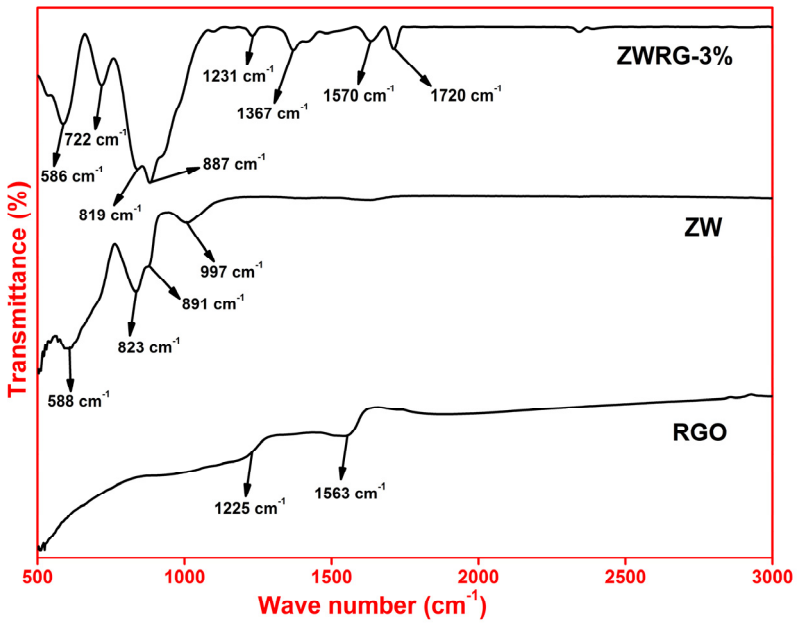

Figure 3. FTIR spectra of RGO, ZW and ZWRG-3% nanocomposites.

XPS survey spectra of ZWRG-3% (Figure 4) exhibits the elemental peaks for C, Zn, W and O, respectively.

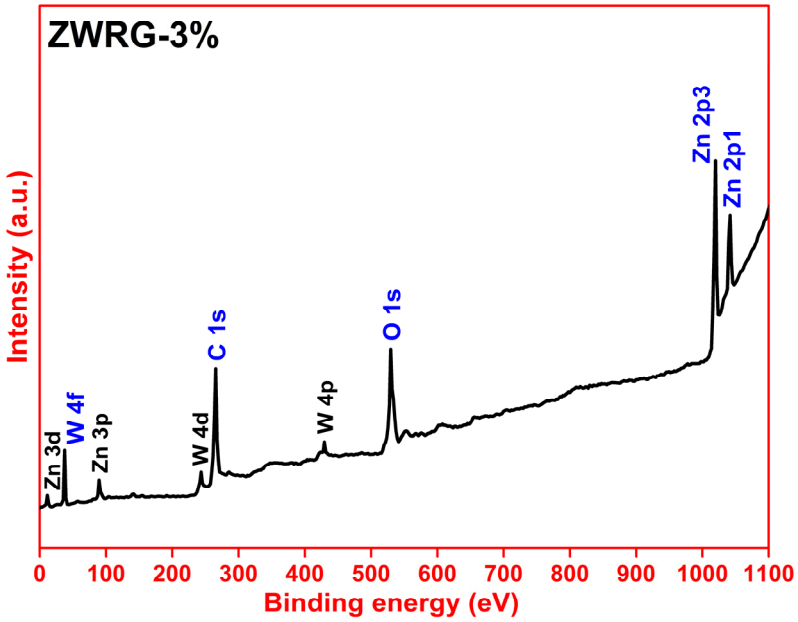

Figure 4. XPS survey spectra of ZWRG-3% nanocomposite.

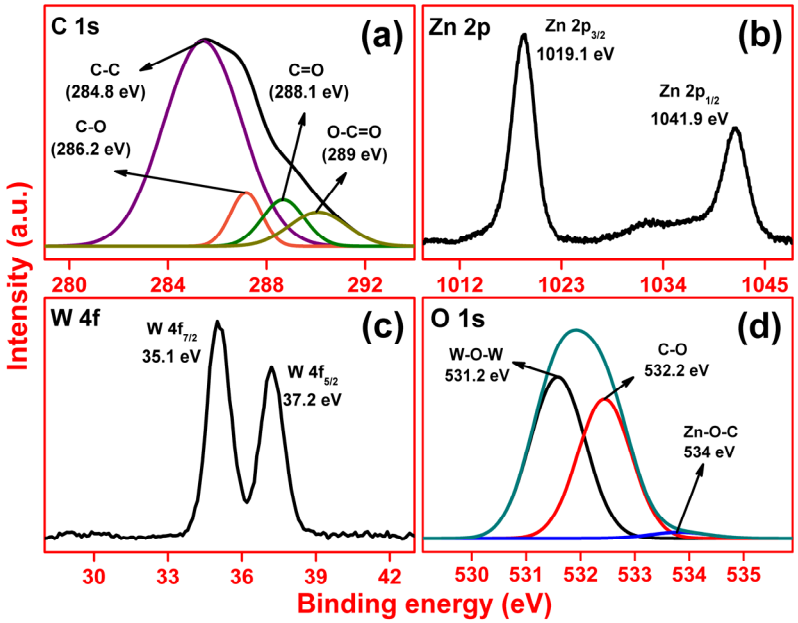

Figure 5. High resolution XPS spectra of (a) C 1s, (b) Zn 2p, (c) W 4f and (d) O 1s of ZWRG-3% nanocomposite.

The high resolution deconvoluted C 1s spectra (Figure 5a) shows four peaks located at 284.7 eV, 286.7 eV, 288.4 eV and 290.1 eV, which can be attributed to the C–C (sp^2 bonded carbon), C–O (hydroxyls), C=O (carbonyls) and O–C=O (carboxyl) groups respectively. The reduced intensities of oxygenated peaks suggest that the GO has been sufficiently reduced to RGO [19]. The C 1s spectra

of GO is given in Figure S2 [ESI] for comparison. The high-resolution Zn 2p spectra shown in Figure 5b consist of two peaks at 1018.9 eV and 1041.8 eV which corresponds to the Zn $2p_{3/2}$ and Zn $2p_{1/2}$ belongs to the Zn^{2+} ions on $ZnWO_4$, respectively [20]. The high-resolution W 4f spectra shown in Figure 5c consist of two peaks at 35.1 eV of W $4f_{7/2}$ and 37.2 eV of W $4f_{5/2}$. The difference of 2.1 eV in binding energy shows that it belongs to the W^{+6} ions [21]. Similarly, the high-resolution O 1s spectra shown in Figure 5d consist of three peaks at 531.2 eV, 532.2 eV and 534 eV corresponding to the W–O–W of $ZnWO_4$, hydroxyl/epoxy groups of RGO and Zn–O–C bonds between $ZnWO_4$ and RGO surfaces respectively [22]. Thus, the XPS studies further verifies the interaction between ZW and RGO in the prepared composites complimenting the results of FTIR.

Figure 6 shows the UV-Vis absorption spectrum of GO, RGO, ZW and ZWRG-3% composite. The composite shows higher absorption in the visible range compared to that of GO, RGO and ZW. This may be due to the synergic interactions of RGO and ZW in the composite.

To calculate the band gap of the materials, the Tauc relation [23] given below was used.

$$\alpha h\nu = K\,(h\nu - E_g)^n$$

where, α is the absorption coefficient, hν is the energy of photon, K is a constant, E_g is the band gap of semiconductor (n = 1/2, 2, 3/2 and 3 for direct-allowed, indirect-allowed, direct-forbidden and indirect-forbidden transition). In this experiment, the direct band gap for pure ZW and ZWRG-3% nanocomposite was calculated by making use of $(\alpha h\nu)^2$ vs. hν plot (inset of Figure 6). The measured band gaps are 3.35 eV and 3.0 eV for ZW and ZWRG-3% nanocomposite respectively.

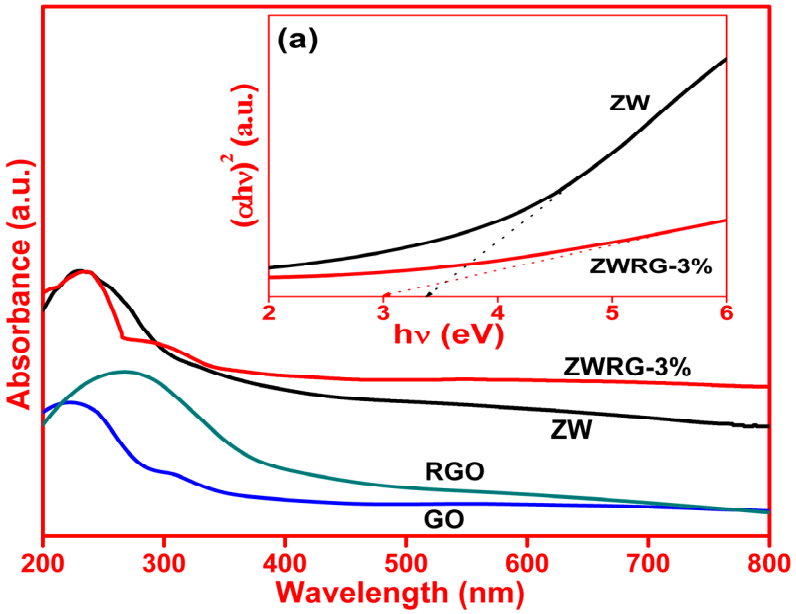

Figure 6. Absorbance spectra for GO, RGO, ZW and ZWRG-3% nanocomposite and Tauc plots (a) for pure ZW and ZWRG-3% nanocomposite.

The reduction in the band gap may be attributed to the delocalization of surface charges resulted by the interactions of RGO in the composite. It is believed that such interactions lead to the formation of new molecular orbitals of lower energy which in turn facilitates the reduction in the bandgap. Such observations for semiconductor composites are reported in the

literature [9,11,24,25,26]. May be more detailed investigations are required to arrive at precise conclusions on the mechanism of this process. The unique light absorbance performance of the binary composites in the visible light region is of great importance for its photocatalytic application since it can be easily activated by visible light [26].

PL spectra of ZW and ZWRG-3% nanocomposites are measured using an excitation wavelength of about 380 nm (Figure 7). The PL emission peak was observed at wavelength of 441 nm for ZW material. However, after the addition of RGO, the intensity of emission peak is significantly decreased. This is due to transfer of electrons from the ZW conduction band to RGO sheets leading to the separation of electron-hole pairs and quenching of luminescence [27]. The results suggest that the combination of RGO and ZW in the composite brings about the synergistic activity in the prepared nanocomposite towards the separation of electron hole pairs and in turn prevents the recombination of photoinduced electron hole pairs facilitating the further energy absorption and enhanced catalytic photodegradation of the substrate [28].

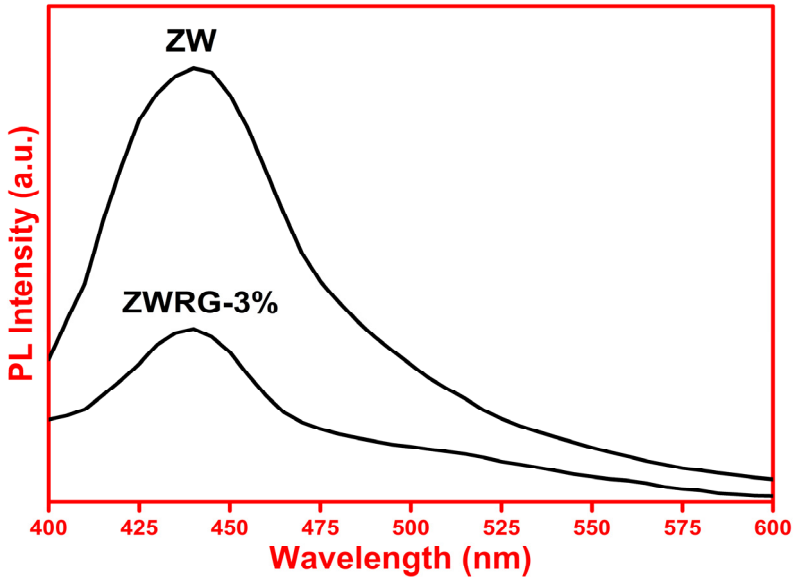

Figure 7. PL spectra for pure ZW and ZWRG-3% nanocomposite.

3.2. Photocatalytic Degradation of MB

MB was taken as a model dye to evaluate the photocatalytic degradation performance of ZWRG nanocomposites. Before switching on the visible light source, the suspension of MB and ZWRG was stirred for 30 minutes in order to achieve the absorption and desorption equilibrium between MB and ZWRG. The result of photocatalytic degradation of MB using ZWRG nanocomposites, with varied concentration of RGO suggests that there is significant enhancement in efficiency compared to pure ZW (Figure 8). In the absence of catalyst there was no change in the concentration of MB even after 150 minutes indicating that self-degradation of MB is negligible and that the degradation occurs only with the aid of the photocatalysts. It is observed that RGO is essential for increasing the efficiency of photocatalytic activities of ZW. Even with a small quantity of RGO (ZWRG-1%) the photocatalytic degradation efficiency increases extensively. With increase in the RGO content, initially the

efficiency of photocatalytic activity increases (up to 3%) and decreases then onwards. When the quantity of RGO is 3%, the nanocomposite showed higher efficiency compared to other samples. The photocatalytic degradation efficiencies are 8.27%, 19.37%, 63.46%, 72.23%, 79.20%, 82.85% and 76.68% for Blank (MB), RGO, ZW, ZWRG-1%, ZWRG-2%, ZWRG-3%, and ZWRG-4%, respectively. The decrease in the activity above 3% RGO content may be ascribed to the coverage of RGO on ZW and hence preventing the latter from effective absorption of incident light radiation and causing low activity [29]. The results are also compared with reported $ZnWO_4$ based ones and other nanocomposites (Table S1).

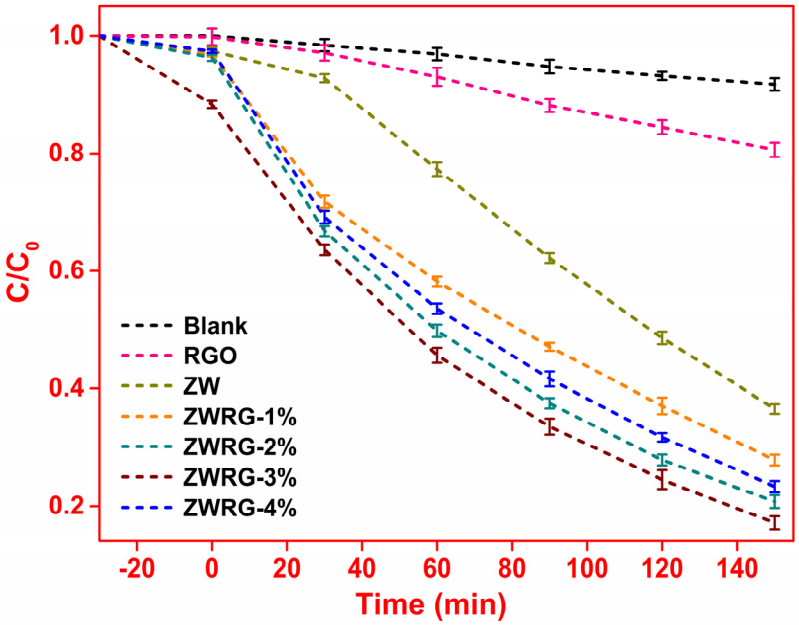

Figure 8. Photocatalytic degradation of MB dye.

The bar diagram given in Figure 9 shows pseudo first-order rate constants for the photocatalytic degradation of MB dye calculated according to the equation,

$$\ln (C_0/C) = -kt$$

where, C_0 is the initial concentration, C is the concentration at irradiation time (t) and k is the first order rate constants. k value was measured from slope of the linear line. The rate constants for photocatalytic degradation (Figure 8) are 0.006 min^{-1}, 0.0013 min^{-1}, 0.005 min^{-1}, 0.009 min^{-1}, 0.0114 min^{-1}, 0.0127 min^{-1} and 0.0103 min^{-1} for Blank (MB), RGO, ZW, ZWRG-1%, ZWRG-2%, ZWRG-3%, and ZWRG-4% respectively. The results show that ZWRG-3% exhibit highest rate constant for photocatalytic degradation amongst all the samples towards MB.

Further, the activity of the catalyst towards an anionic dye, methyl orange (MO) and a cationic dye, rhodamine B (RB) has also been studied under the same conditions (Figure S3 and Figure S4). Figure 10 shows the comparison of degradation efficiencies of the catalyst ZWRG-3% on MB, RB and MO. As can be seen from the figure, MB (82.85%) and RB (77.06%) degraded to a greater extent than that of MO (61.81%). The MB and RB being cationic dyes can be adsorbed on to the catalyst surface to a better extent because of the fact that the RGO provides a slightly negatively charged surface. Due to the same reason the MO cannot be adsorbed efficiently on to the catalyst

surface and this has resulted in the observed variation in the degradation of the dyes. The lesser degradation of RB compared to MB may be due to its larger molecular size compared to the former. The efficiency of the catalyst has also been compared with commercial P25 photocatalyst using MB as the substrate. The performance of ZWRG-3% is found to be much better than that of commercial P25 (Figure S5 and Figure S6) and those reported in the literature [30,31].

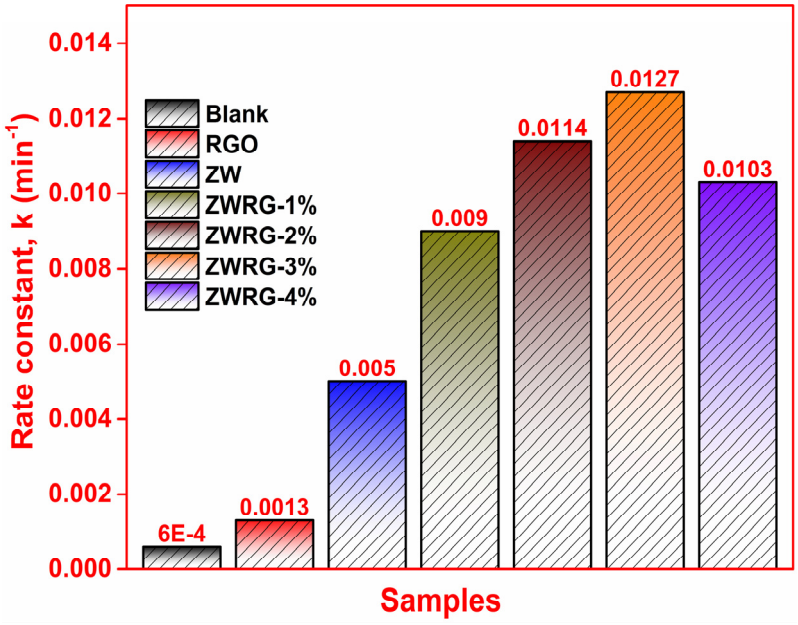

Figure 9. First order rate constants for the degradation of MB dye.

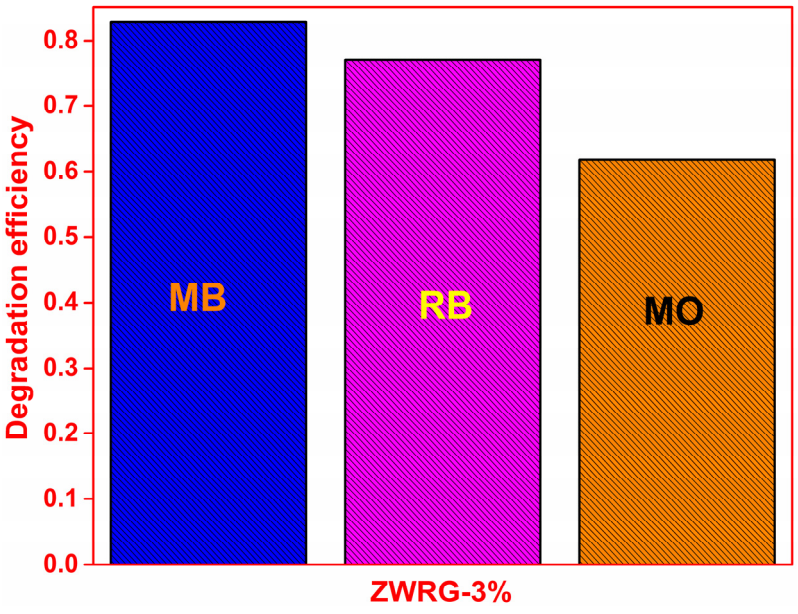

Figure 10. Comparison of degradation efficiency of ZWRG-3% over different dyes.

The stability and reusability of the catalyst is an important factor for practical applications. The catalyst ZWRG-3% is tested for this property and Figure 11, shows the first five continuous cycles of its performance. As can be observed from the figure, the catalyst has good stability and reusability.

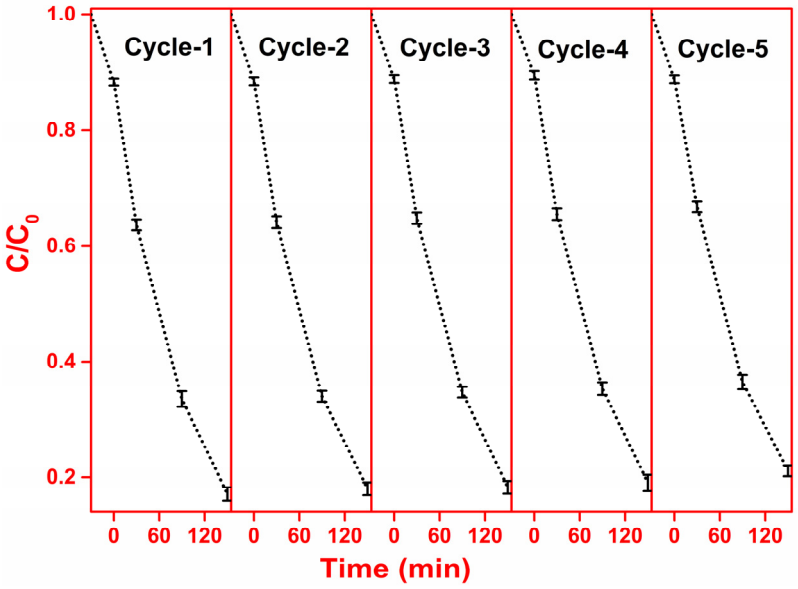

Figure 11. Plot of C/C_0 vs. time for ZWRG-3% with MB over five cycles.

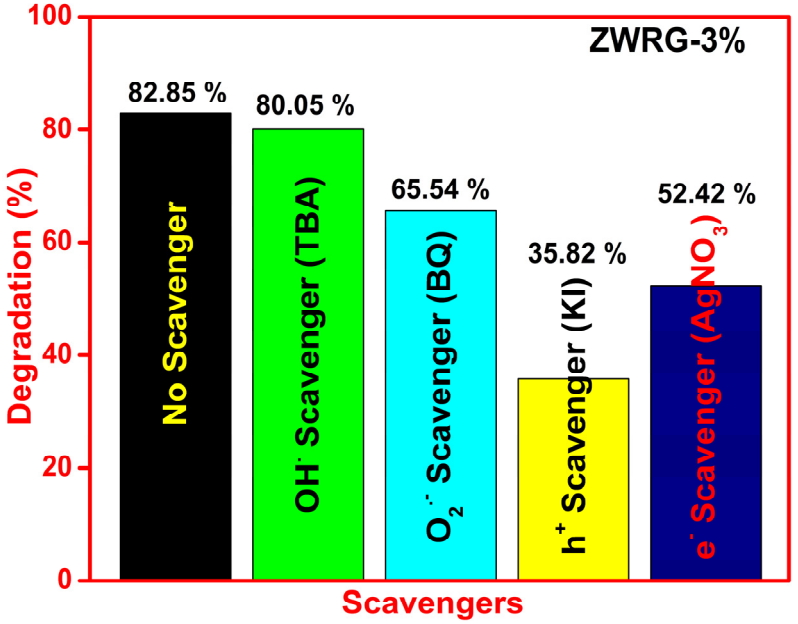

Figure 12. Effect of scavengers for ZWRG-3% nanocomposite.

To identify the major active species of the photocatalytic reactions, the trapping experiments are carried out under the conditions followed for regular photocatalytic degradation processes. Quenchers consisting of benzoquinone (1 mM, BQ) as a scavenger for $O_2\cdot^-$, potassium iodide (10 mM, KI) as a scavenger of h^+, silver nitrate (10 mM, $AgNO_3$) as a scavenger of e^- and ternary

butanol (10 mM, TBA) as a scavenger of OH· are added to the MB solution before the addition of nanocomposite to determine the presiding active species and the obtained results are given in Figure 12. As can be understood from the results, in this case, hydroxyl radicals are not the main active species. This is because the corresponding scavenger TBA did not decrease the photo degradation efficiency appreciably. Whereas, the addition of KI (holes scavenger) decreased the rate drastically suggesting that holes are the major active species here followed by electrons and superoxide radical anions, $O_2{\cdot}^-$.

The schematic representation of the mechanism of photocatalytic degradation of MB dye by the ZWRG-3% nanocomposite is shown in Figure 13. In the case of neat ZW, excitation by visible light irradiation is not possible due to its wide energy gap. However, when RGO is introduced, the interactions between ZW and RGO decrease the band gap of the composite enabling it to absorb the visible light and to excite the electrons from VB to CB. The excited electrons in CB and the holes in the VB would get separated efficiently and easily get transferred via RGO interlayer and subsequently react with water and oxygen to generate hydroxyl and superoxide radicals. The radicals would subsequently oxidize the MB to harmless degraded products.

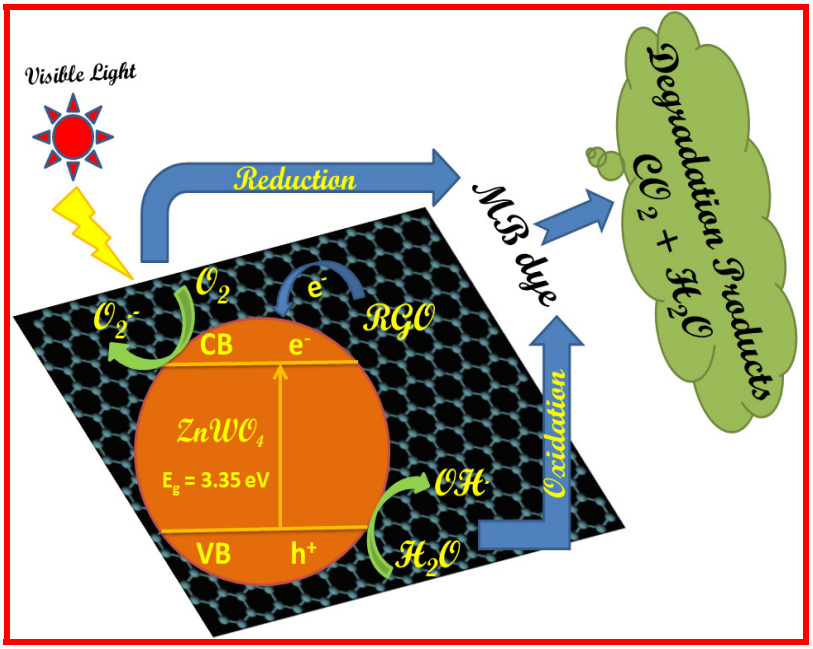

Figure 13. Photocatalytic degradation mechanism for MB by ZWRG-3% nanocomposite.

4. Conclusions

A facile microwave method has been used to synthesize ZWRG nanocomposites. The phase structure, surface morphology and optical properties of the as-synthesized nanocomposites were studied through XRD, FTIR, TEM, EDX, XPS, PL and UV-Visible spectroscopic techniques. The visible light photocatalytic degradation studies of MB with the nanocomposites revealed that the ZWRG-3% nanocomposite exhibits higher performance. The high efficiency of this catalyst is ascribed to the synergic effect of RGO sheets with ZW. The activity was much better than the commercial P25 photocatalyst. Further, the ZWRG-3% nanocomposite catalyst has excellent

stability and reusability which can make it a promising eco-friendly catalyst for degradation of dyes or for wastewater treatment.

Acknowledgment

M.J.S.M. is grateful to the National Institute of Technology Karnataka-Surathkal, Mangalore, for the award of Institute fellowship.

Conflict of Interest

Authors declare that there is not conflict of interest.

References

1. Blackburn RS (2004) Natural polysaccharides and their interactions with dye molecules: applications in effluent treatment. *Environ Sci Technol* 38: 4905–4909.
2. Ma J, Song W, Chen C, et al. (2005) Fenton degradation of organic compounds promoted by dyes under visible irradiation. *Environ Sci Technol* 39: 5810–5815.
3. Mills A, Le Hunte S (1997) An overview of semiconductor photocatalysis. *J Photoch Photobio A* 108: 1–35.
4. Born P, Robertson D, Smith P, et al. (1981) The preparation and scintillation properties of zinc tungstate single crystals. *J Lumin* 24: 131–134.
5. Tien HN, Khoa NT, Hahn SH, et al. (2013) One-pot synthesis of a reduced graphene oxide-zinc oxide sphere composite and its use as a visible light photocatalyst. *Chem Eng J* 229: 126–133.
6. Huang X, Qi X, Boey F, et al. (2012) Graphene-based composites. *Chem Soc Rev* 41: 666–686.
7. Xiang Q, Yu J, Jaroniec M (2012) Graphene-based semiconductor photocatalysts. *Chem Soc Rev* 41: 782–796.
8. Wang W, Shen J, Li N, et al. (2013) Synthesis of novel photocatalytic RGO-$ZnWO_4$ nanocomposites with visible light photoactivity. *Mater Lett* 106: 284–286.
9. Sadiq MMJ, Shenoy US, Bhat DK (2016) Novel RGO-$ZnWO_4$-Fe_3O_4 nanocomposite as high performance visible light photocatalyst. *RSC Adv* 6: 61821–61829.
10. Sadiq MMJ, Nesaraj AS (2015) Soft chemical synthesis and characterization of $BaWO_4$ nanoparticles for photocatalytic removal of Rhodamine B present in water sample. *J Nanostruct Chem* 5: 45–54.
11. Sadiq Mohamed MJ, Bhat Denthaje K (2016) Novel RGO-$ZnWO_4$-Fe_3O_4 nanocomposite as an efficient catalyst for rapid reduction of 4-nitrophenol to 4-aminophenol. *Ind Eng Chem Res* 55: 7267–7272.
12. Hummers Jr WS, Offeman RE (1958) Preparation of graphitic oxide. *J Am Chem Soc* 80: 1339–1339.
13. Huang G, Shi R, Zhu Y (2011) Photocatalytic activity and photoelectric performance enhancement for $ZnWO_4$ by fluorine substitution. *J Mol Catal A-Chem* 348: 100–105.
14. Rahimi Nasrabadi M, Pourmortazavi SM, Ganjali MR, et al. (2013) Electrosynthesis and characterization of zinc tungstate nanoparticles. *J Mol Struct* 1047: 31–36.
15. Raja K, Verma S, Karmakar S, et al. (2011) Synthesis and characterization of magnetite nanocrystals. *Cryst Res Technol* 46: 497–500.

16. Huang G, Zhu Y (2007) Synthesis and photocatalytic performance of $ZnWO_4$ catalyst. *Mater Sci Eng B* 139: 201–208.
17. Nethravathi C, Nisha T, Ravishankar N, et al. (2009) Graphene-nanocrystalline metal sulphide composites produced by a one-pot reaction starting from graphite oxide. *Carbon* 47: 2054–2059.
18. Szabó T, Berkesi O, Dékány I (2005) DRIFT study of deuterium-exchanged graphite oxide. *Carbon* 43: 3186–3189.
19. Jiang N, Xiu Z, Xie Z, et al. (2014) Reduced graphene oxide-CdS nanocomposites with enhanced visible-light photoactivity synthesized using ionic-liquid precursors. *New J Chem* 38: 4312–4320.
20. Atuchin VV, Galashov EN, Khyzhun OY, et al. (2011) Structural and electronic properties of $ZnWO_4$ (010) cleaved surface. *Cryst Growth Des* 11: 2479–2484.
21. Cortés Jácome M, Angeles Chavez C, Lopez Salinas E, et al. (2007) Migration and oxidation of tungsten species at the origin of acidity and catalytic activity on WO_3-ZrO_2 catalysts. *Appl Catal A-Gen* 318: 178–189.
22. Sun L, Zhao X, Jia CJ, et al. (2012) Enhanced visible-light photocatalytic activity of gC_3N_4-$ZnWO_4$ by fabricating a heterojunction: investigation based on experimental and theoretical studies. *J Mater Chem* 22: 23428–23438.
23. Tauc J, Grigorovici R, Vancu A (1966) Optical properties and electronic structure of amorphous germanium. *Phys Status Solidi (B)* 15: 627–637.
24. Jiang Y, Wang WN, et al. (2014), Facile Aerosol Synthesis and Characterization of Ternary Crumpled Graphene-TiO_2-Magnetite Nanocomposites for Advanced Water Treatment. *ACS Appl Mater Inter* 6: 11766–11774.
25. Sun M, Fang Y, Wang Y, et al. (2015) Synthesis of Cu_2O/graphene/rutile TiO_2 nanorod ternary composites with enhanced photocatalytic activity. *J Alloy Compd* 650: 520–527.
26. Luo QP, Yu XY, Lei BX, et al. (2012) Reduced graphene oxide-hierarchical ZnO hollow sphere composites with enhanced photocurrent and photocatalytic activity. *J Phys Chem C* 116: 8111–8117.
27. Williams G, Kamat PV (2009) Graphene-Semiconductor Nanocomposites: Excited-State Interactions between ZnO Nanoparticles and Graphene Oxide. *Langmuir* 25: 13869–13873.
28. Wang L, Ding J, Chai Y, et al. (2015) CeO_2 nanorod/gC_3N_4/N-rGO composite: enhanced visible-light-driven photocatalytic performance and the role of N-rGO as electronic transfer media. *Dalton Trans* 44: 11223–11234.
29. Pradhan GK, Padhi DK, Parida K (2013) Fabrication of α-Fe_2O_3 nanorod/RGO composite: a novel hybrid photocatalyst for phenol degradation. *ACS Appl Mater Inter* 5: 9101–9110.
30. Lavanya T, Dutta M, Satheesh K (2016) Graphene wrapped porous tubular rutile TiO_2 nanofibers with superior interfacial contact for highly efficient photocatalytic performance for water treatment. *Sep Purif Technol* 168: 284–293.
31. Lavanya T, Satheesh K, Dutta M, et al. (2014) Superior photocatalytic performance of reduced graphene oxide wrapped electrospun anatase mesoporous TiO_2 nanofibers. *J Alloy Compd* 615: 643–650.

AIMS Press